

# Noise Reduction of Stochastic Density Functional Theory for Metals

Jake P. Vu<sup>a)</sup> and Ming Chen<sup>b)</sup>

*Department of Chemistry, Purdue University, West Lafayette, Indiana 47906, USA*

(Dated: 8 March 2024)

Density Functional Theory (DFT) has become a cornerstone in the modeling of metals. However, accurately simulating metals, particularly under extreme conditions, presents two significant challenges. First, simulating complex metallic systems at low electron temperatures is difficult due to their highly delocalized density matrix. Second, modeling metallic warm-dense materials at very high electron temperatures is challenging because it requires the computation of a large number of partially occupied orbitals. This study demonstrates that both challenges can be effectively addressed using the latest advances in linear-scaling stochastic DFT methodologies. Despite the inherent introduction of noise into all computed properties by stochastic DFT, this research evaluates the efficacy of various noise reduction techniques under different thermal conditions. Our observations indicate that the effectiveness of noise reduction strategies varies significantly with the electron temperature. Furthermore, we provide evidence that the computational cost of stochastic DFT methods scales linearly with system size for metal systems, regardless of the electron temperature regime.

## I. INTRODUCTION

Metals are ubiquitous in daily life, industry, and academic research, due to their unique mechanical, magnetic, and electronic properties<sup>1–3</sup>. Theoretical modeling of metal electronic structures is crucial for understanding their ground and excited state properties<sup>4,5</sup>. Density functional theory (DFT) is a widely used approach in materials science and condensed matter physics to accurately model the ground-state properties of metals at reasonable computational costs.<sup>4,6,7</sup> Recent studies have focused on complex metal systems such as metal nanostructures, high-entropy alloys, and metal-support interfaces, which exhibit intriguing properties and have significant applications<sup>8–10</sup>. These materials often require large supercells in theoretical modeling, sometimes containing more than 1000 atoms<sup>11–13</sup>. While DFT has been effective for studying bulk metal systems, the computational cost of conventional DFT scales as  $O(N_e^3)$ , where  $N_e$  represents the number of electrons. This makes the application of conventional DFT methods to complex metal systems challenging.

Another significant challenge arises in modeling metallic systems at high electron temperatures, especially in the context of warm-dense materials relevant to fusion energy<sup>14</sup>. Accurate modeling of these materials requires the description of electronic structure at extremely high electron temperatures<sup>15</sup>. Conventional DFT methods face difficulties in modeling warm dense materials due to the requirement of a large number of partially occupied orbitals<sup>16</sup>. Therefore, the development of DFT methodologies that can minimize computational expenses is essential for modeling metals across various system sizes and under different conditions.

Various linear-scaling DFT methods have been developed to address the computational challenges associated with modeling complex materials<sup>17–26</sup>. These methods generally employ one of two strategies: exploiting the “nearsightedness” of the electronic structure, or decomposing the system into smaller, manageable subsystems<sup>19,24,26–29</sup>. The concept of

nearsightedness in electronic structure implies that the one-body density matrix,  $\rho(\mathbf{r}, \mathbf{r}')$ , decays exponentially with the distance between points  $\mathbf{r}$  and  $\mathbf{r}'$ <sup>30,31</sup>. This property allows for the truncation of the density matrix, facilitating the use of sparse matrix techniques to achieve linear-scaling computational efficiency<sup>32,33</sup>. Such an approach is particularly effective for systems with a large band gap or metallic systems at high electron temperatures<sup>32,34</sup>. However, challenges arise when dealing with metals at low electron temperatures due to the slow decay of  $\rho(\mathbf{r}, \mathbf{r}')$ , making the application of this principle less straightforward<sup>35,36</sup>. Alternatively, some methods focus on the subsystem decomposition approach, which relies on embedding theory to account for interactions between a subsystem and its environment<sup>17</sup>. This technique has shown success with non-covalently bonded systems, such as molecular clusters<sup>24</sup>, but faces significant challenges when applied to inorganic materials with covalent bonds<sup>37</sup>. Notwithstanding, certain linear-scaling DFT methods have demonstrated the ability to efficiently model metals with high electron temperatures by focusing on a localized density matrix. Nonetheless, these methods often struggle to access high-energy orbital information, which remains a limitation<sup>18,38,39</sup>.

Stochastic DFT (sDFT) represents a significant advancement in linear-scaling DFT methodologies, uniquely addressing challenges posed by systems characterized by small or negligible fundamental gaps<sup>40</sup>. Unlike traditional DFT approaches that depend on the Kohn-Sham (KS) orbitals, sDFT calculates ground-state properties—including electron density, ground-state energy, and forces on nuclei—through the statistical averaging over a set of stochastic orbitals. Research into the application of sDFT on semiconductor materials has revealed a particularly compelling advantage: the number of stochastic orbitals required for accurate property calculation does not scale with the size of the system. This characteristic enables sDFT to achieve linear or even sublinear scaling efficiency for computations of electron density, energy per particle, and nuclear forces. The independence from explicit KS orbitals allows sDFT to effectively model systems at high electron temperatures, such as warm-dense materials (WDM), with enhanced computational efficiency<sup>39,41–43</sup>.

Inherent to sDFT, stochastic noise affects all calculated

<sup>a)</sup>Electronic mail: vuj@purdue.edu

<sup>b)</sup>Electronic mail: chen4116@purdue.edu

properties, presenting a significant computational challenge. To reduce this noise by an order of magnitude, the number of stochastic orbitals must be increased by two orders of magnitude, leading to a substantial rise in computational demand<sup>44</sup>. To mitigate this issue, a variety of noise reduction techniques have been developed, each leveraging different approaches to enhance computational efficiency without compromising accuracy. Among these, “overlapped embedded-fragmented sDFT” (o-efsDFT) which is based on real-space fragmentation technique (oef-sDFT)<sup>45</sup>, “energy-window sDFT” (ew-sDFT) which is an energy-space fragmentation method<sup>44</sup>, and “energy window embedded-fragmented sDFT” (ew-efsDFT) which uses a hybrid strategy<sup>46</sup> have shown promise. These methods facilitate the study of semiconductors, including those with minimal band gaps, by effectively managing stochastic noise and computational workload. Despite their success with semiconductors, the application of these noise reduction techniques to metals, particularly at varying electron temperatures, remains an area with limited exploration<sup>42</sup>.

In this study, we undertake a comprehensive benchmarking of noise reduction techniques in stochastic Density Functional Theory (sDFT), aimed at efficiently modeling metals subjected to both low and high electron temperatures. Our paper is structured to facilitate a clear understanding of these techniques and their efficacy. We begin by offering a concise introduction to sDFT, alongside a detailed overview of the various noise reduction strategies that have been developed to date. This sets the foundation for our subsequent analysis. Following the introduction, we delve into an empirical evaluation of these noise reduction techniques, using bulk aluminum as our test system. This evaluation encompasses simulations at both room temperature and elevated temperatures, providing insights into the performance of these methods across a range of thermal conditions. Additionally, we extend our analysis to compare the computational costs associated with the ew-efsDFT method across different system sizes and temperatures. This comparison aims to elucidate the scalability and efficiency of ew-efsDFT, offering valuable perspectives on its practical application in materials science research. Through this structured approach, our study aims to illuminate the capabilities and limitations of noise reduction techniques in sDFT, contributing to the ongoing optimization of computational methodologies for the modeling of metal systems under diverse thermal conditions.

## II. STOCHASTIC DENSITY FUNCTIONAL THEORY

We initiate our discussion with a consideration of a supercell of volume  $V$ , encompassing an electron density  $\rho(\mathbf{r})$  that is discretized over a real-space grid consisting of  $N_G$  grid points. For the scenario of spin-unpolarized systems, the electron density is expressed as:

$$\rho(\mathbf{r}) = 2\sum_i f(\varepsilon_i) \langle \mathbf{r} | \psi_i \rangle \langle \psi_i | \mathbf{r} \rangle \quad (1)$$

where  $\psi_i(\mathbf{r}) = \langle \mathbf{r} | \psi_i \rangle$  represents the Kohn-Sham (KS) orbitals, and  $\varepsilon_i$  denotes the corresponding KS orbital energies, according to the Kohn-Sham formulation of DFT. The function  $f(x)$ ,

serving as a smearing function to accommodate the occupancy of states, is crucial for DFT calculations in metallic systems. Specifically, we employ the Fermi-Dirac distribution:

$$f(x; \mu, \beta) = \frac{1}{1 + e^{\beta(x-\mu)}} \quad (2)$$

with  $\mu$  symbolizing the chemical potential, and  $\beta = 1/k_B T$  representing the inverse temperature factor, where  $k_B$  is the Boltzmann constant and  $T$  denotes the electron temperature. It is pertinent to highlight that alternative smearing functions, such as the error function, are equally viable for implementation within the scope of sDFT. The Kohn-Sham Hamiltonian,  $\hat{h}_{KS}$ , is defined as:

$$\hat{h}_{KS} = \hat{t} + \hat{v}_{loc} + \hat{v}_{nl} + \hat{v}_H + \hat{v}_{XC}, \quad (3)$$

where  $\hat{t}$  delineates the kinetic energy term,  $\hat{v}_{loc}$  and  $\hat{v}_{nl}$  correspond to the local and nonlocal pseudopotentials, respectively,  $\hat{v}_H$  represents the Hartree potential, and  $\hat{v}_{XC}$  denotes the exchange-correlation potential. Consequently, the one-body reduced density matrix is succinctly described by  $\hat{\rho} = f(\hat{h}_{KS}; \mu, \beta)$ .

In sDFT, the electron density  $\rho(\mathbf{r})$  is calculated using stochastic orbitals  $|\chi\rangle$  as follows:

$$\rho(\mathbf{r}) = \langle \langle \chi | \hat{\rho} \delta(\mathbf{r} - \hat{\mathbf{r}}) | \chi \rangle \rangle_{\chi} = \langle |\xi(\mathbf{r})|^2 \rangle_{\chi}, \quad (4)$$

where  $\delta(\cdot)$  is the Dirac delta function, and  $|\xi\rangle = \sqrt{\hat{\rho}} |\chi\rangle$  represents a projected stochastic orbital. The notation  $\langle \dots \rangle_{\chi}$  denotes averaging over all samples of  $\chi$ . In practical sDFT calculations, a finite number ( $N_{\chi}$ ) of stochastic orbitals is employed. The stochastic orbital  $\chi(\mathbf{r})$  is constructed to satisfy  $\langle \chi(\mathbf{r})^* \chi(\mathbf{r}') \rangle_{\chi} = \delta(\mathbf{r} - \mathbf{r}')$ . Practically,  $\chi(\mathbf{r}) = \pm(\Delta V)^{-\frac{1}{2}}$ , where  $\Delta V = V/N_G$  is the volume element of the real-space grid, and the sign of  $\chi$  is randomly, uniformly, and independently selected for each grid point. Equation 4 becomes exact in the limit as the number of stochastic orbitals  $N_{\chi} \rightarrow \infty$ ; otherwise, the density obtained is a stochastic approximation.

The projection of stochastic orbitals onto the operator  $\sqrt{\hat{\rho}}$  can be efficiently approximated by expanding  $\sqrt{f(\hat{h}_{KS}; \mu, \beta)}$  through polynomial series, such as Chebyshev or Newton’s Interpolation polynomials<sup>47,48</sup>. Specifically, this approximation takes the form:

$$\sqrt{f(\hat{h}_{KS}; \mu, \beta)} \approx \sum_{n=0}^{N_c} a_n(\mu, \beta) T_n(\hat{h}_{KS}), \quad (5)$$

where  $N_c$  denotes the length of the polynomial chain, and  $T_n(\cdot)$  are the Chebyshev polynomials. Within the framework of sDFT, the application of  $T_n(\hat{h}_{KS})$  to a stochastic orbital is computed utilizing the iterative formula associated with Chebyshev polynomials, thereby facilitating a computationally efficient projection algorithm.

A property  $O$ , other than electron density, can be calculated as follows. If  $O$  is an explicit functional of electron density, it can be calculated using  $\rho$  from Eq. (4). Otherwise,  $O$  requires calculating the trace of an operator, which can be evaluated by

the stochastic trace formula. In the stochastic trace formula, the trace of an operator  $\hat{O}[\rho]$  is calculated with

$$\text{Tr}(\hat{O}[\rho]) = \langle\langle \chi | \hat{O}[\rho] | \chi \rangle\rangle_{\chi}. \quad (6)$$

Here,  $\hat{O}[\rho]$  indicates that  $\hat{O}$  depends on the electron density  $\rho$ . In a special case,  $\hat{O}[\rho] = \hat{\rho}[\rho]\hat{A}$ , where  $\hat{A}$  is a one-body operator. In this case,

$$O = 2\text{Tr}(\hat{\rho}\hat{A}) = 2\langle\langle \xi | \hat{A} | \xi \rangle\rangle_{\chi}. \quad (7)$$

For some other properties,  $\hat{O}$  is more complicated. For example, sDFT uses the following formula to calculate the electron density of states at energy  $\varepsilon$ :

$$D(\varepsilon) = \langle\langle \chi | \delta(\hat{h}_{\text{KS}} - \varepsilon) | \chi \rangle\rangle_{\chi} \approx \langle\langle \chi | G(\hat{h}_{\text{KS}}; \varepsilon, \sigma) | \chi \rangle\rangle_{\chi}, \quad (8)$$

where  $G(x; \varepsilon, \sigma) = \frac{1}{\sqrt{2\pi\sigma^2}} e^{-(x-\varepsilon)^2/2\sigma^2}$  is a Gaussian function. A pre-selected  $\sigma$  is the broadening of the Gaussian function, which determines the broadening of the density of states. The second example, electron entropy ( $S_{\text{KS}}$ ), is essential for finite temperature calculations involving metals. In sDFT,  $S_{\text{KS}}$  can be calculated using the formula:

$$S_{\text{KS}} = -2k_{\text{B}} \langle\langle \chi | \hat{\rho} \log \hat{\rho} + (\hat{I} - \hat{\rho}) \log(\hat{I} - \hat{\rho}) | \chi \rangle\rangle_{\chi}, \quad (9)$$

where  $\hat{I}$  represents the identity operator. Both Eq. (8) and Eq. (9) can be calculated with a Chebyshev polynomial expansion, similar to Eq. (5).

Due to the use of finite stochastic orbitals  $|\chi\rangle$ , noise exists in all quantities calculated with sDFT. This noise varies inversely with the square root of the number of stochastic orbitals,  $N_{\chi}$ , in accordance with the central limit theorem. Specifically, to reduce the stochastic fluctuation by one order of magnitude, it is necessary to increase  $N_{\chi}$  by two orders of magnitude. Therefore, noise reduction techniques are crucial for accurately determining properties without compromising the efficiency of sDFT. It is important to note that for many observables, such as electron density, density of states, and atomic forces, the noise does not scale with the system size. This allows sDFT to maintain linear scaling. Conversely, for properties like the energy per particle, the noise diminishes as the system size increases. This implies that fewer stochastic orbitals are required for larger systems, making sDFT a sub-linear-scaling method. However, for total energy calculations, noise amplifies with system size, challenging the linear-scaling property of sDFT. Users are encouraged to carefully assess the properties they intend to calculate with sDFT, considering the method's scalability and noise characteristics for their specific application.

### A. Overlapped Embedded Fragmentation

Reduction in the statistical noise can be achieved by introduction of a reference system that can be calculated by deterministic KS-DFT. This will provide us a reasonable approximation of the electron density matrix which is corrected with sDFT. One way to generate such reference system is

to decompose the whole system into overlapped fragments, leading to the implementation of the overlapped embedded-fragmented stochastic DFT (o-efsDFT). We will outline the method in the rest of this section.

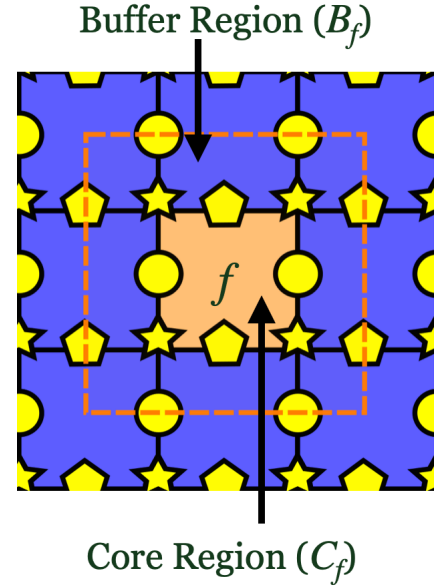


FIG. 1. Schematic for overlapped fragmentation is shown in this figure.<sup>21</sup> The system is divided into overlapped fragments. Each fragment  $f$  is composed of a core region ( $C_f$ ) and a buffer region ( $B_f$ ) is defined around each  $C_f$ . A deterministic DFT is performed for each dressed fragment ( $D_f$ ), which is the union of  $C_f$  and  $B_f$  ( $C_f \cup B_f$ )

The o-efsDFT method divides a supercell into fragments referred to as core regions ( $C_f$ ) that is wrapped by a buffer region ( $B_f$ ) to create a dressed fragment ( $D_f = C_f \cup B_f$ , where  $f$  is the fragment index). The fragment density matrix,  $\hat{\rho}_f$ , is defined as

$$\langle \mathbf{r} | \hat{\rho}_f | \mathbf{r}' \rangle = \begin{cases} \sum_{i=1}^f \sqrt{f(\varepsilon_i^f; \mu_f, \beta)} \langle \mathbf{r} | \varphi_i^f \rangle \langle \varphi_i^f | \mathbf{r}' \rangle, & \mathbf{r}' \in D_f \\ 0, & \mathbf{r}' \notin D_f \end{cases} \quad (10)$$

where  $\varphi_i^f$  are the KS orbitals for the  $f$ 'th fragment obtained from deterministic KS-DFT.  $\varepsilon_i^f$  are fragment KS orbital energies.  $\mu_f$  is the chemical potential that keeps each fragment charge neutral. We want to emphasize that using o-efsDFT to model a charge-separated system needs further developments. In o-efsDFT, electron density is calculated by

$$\rho(\mathbf{r}) = 2 \sum_f \rho_f(\mathbf{r}) + 2 \langle |\xi(\mathbf{r})|^2 \rangle_{\chi} - 2 \sum_f \langle |\xi_f(\mathbf{r})|^2 \rangle_{\chi}, \quad (11)$$

where the fragment electron density is  $\rho_f(\mathbf{r}) = \sum_{i=1}^f f(\varepsilon_i^f, \mu_f, \beta) |\varphi_i^f(\mathbf{r})|^2$ ,  $\xi_f(\mathbf{r}) = \sum_{i=1}^f \sqrt{f(\varepsilon_i^f, \mu_f, \beta)} \varphi_i^f(\mathbf{r}) \langle \varphi_i^f | \chi \rangle_{D_f}$ , and  $\langle \varphi_i^f | \chi \rangle_{D_f} = \int_{D_f} d\mathbf{r} \varphi_i^f(\mathbf{r})^* \chi(\mathbf{r})$ . If  $\hat{\rho}_f$  is similar with  $\hat{\rho}$ , noise in the second term of Eq.(11) will almost cancel noise in the third term.

As we will demonstrate later, it is crucial to have a reasonably good fragment density matrix in order to maximizing the noise-reduction efficiency of sDFT.

## B. Energy Windows

Reduction in the stochastic noise can also be achieved by dividing the occupied space into subspaces named as “energy windows”. In this method, instead of projecting the stochastic orbitals onto the occupied space, the stochastic orbitals are projected onto energy windows using a set of projectors,  $\hat{\mathbf{P}}_1, \dots, \hat{\mathbf{P}}_{N_w}$ . Here, the projector  $\hat{\mathbf{P}}_w$  is defined as

$$\hat{\mathbf{P}}_w = f(\hat{h}_{\text{KS}}; e_w, \beta) - f(\hat{h}_{\text{KS}}; e_{w-1}, \beta) \quad (12)$$

for  $1 \leq w \leq N_w$ , where  $-\infty = e_0 < e_1 < \dots < e_{N_w} = \mu$ . In energy windows sDFT (ew-sDFT), the electron density is obtained from the sum of all the projected densities.

$$\rho(\mathbf{r}) = 2 \sum_{w=1}^{N_w} \left\langle \left| \xi^{(w)}(\mathbf{r}) \right|^2 \right\rangle_{\chi} \equiv 2 \sum_{w=1}^{N_w} \rho^{(w)}(\mathbf{r}), \quad (13)$$

where  $\left| \xi^{(w)} \right\rangle = \sqrt{\hat{\mathbf{P}}_w} |\chi\rangle$  is a projected stochastic orbital for window  $w$ .  $\left| \xi^{(w)} \right\rangle$  are calculated simultaneously with a single polynomial expansion.

## C. Energy Window Embedded Fragmentation

The final noise reduction method at our disposal combines the approaches used in o-efsDFT and ew-sDFT with the resulting expression for the electron density on each grid point  $\mathbf{r}$

$$\rho(\mathbf{r}) = 2 \sum_f \rho_f(\mathbf{r}) + 2 \sum_{w=1}^{N_w} \left\langle \left| \zeta^{(w)}(\mathbf{r}) \right|^2 \right\rangle_{\chi} - 2 \sum_f \sum_{w=1}^{N_w} \left\langle \left| \xi_f^{(w)}(\mathbf{r}) \right|^2 \right\rangle_{\chi}, \quad (14)$$

where  $\zeta^{(w)}(\mathbf{r}) = \left\langle \mathbf{r} \left| \sqrt{\hat{\rho} \hat{\mathbf{P}}_w} \right| \chi \right\rangle$  and  $\xi_f^{(w)}(\mathbf{r}) = \left\langle \mathbf{r} \left| \hat{\rho}_f \sqrt{\hat{\mathbf{P}}_w} \right| \chi \right\rangle$ . The projection operators on the energy windows are the same as ew-efsDFT besides the last window is defined as

$$\hat{\mathbf{P}}_{N_w} = \hat{I} - \sum_{w=1}^{N_w-1} \hat{\mathbf{P}}_w, \quad (15)$$

In ew-sDFT,  $\sum_{w=1}^{N_w} \hat{\mathbf{P}}_w$  equals the density matrix  $\hat{\rho}$ , while in ew-efsDFT, it returns the identity operator,  $\hat{I}$ . In addition, the highest energy window is set to  $e_{N_w} = \mu$  in ew-sDFT, while in ew-efsDFT, the energy windows are held fixed for the entire self-consistent procedure and are chosen to be independent of the chemical potential,  $\mu$ . This greatly simplifies the on-the-fly calculations of the chemical potential.<sup>46</sup> The actions of

$\sqrt{\hat{\rho} \hat{\mathbf{P}}_w}$  and  $\sqrt{\hat{\mathbf{P}}_w}$  on  $|\chi\rangle$  are obtained using a Chebyshev polynomial series.  $\rho_f$  is calculated in the same way as o-efsDFT.

## III. RESULTS

sDFT, o-efsDFT, ew-sDFT, and ew-efsDFT were tested on an aluminum crystal of varying supercell sizes. Various temperatures ranging from 300 K to 60,000 K were used to test metal calculations at ambient conditions as well as in warm-dense metal systems. All calculations were performed using the Becke–Lee–Yang–Parr (BLYP) functional<sup>49,50</sup>. It is important to emphasize that an exchange-correlation functional specifically tuned for warm-dense matter should be used to accurately model materials with extremely high electron temperatures<sup>51–53</sup>. However, this work mainly focuses on demonstrating the computational efficiency of various sDFT implementations; thus, the BLYP functional was used in all calculations. A wave function cutoff of 60.0 Ry and a density cutoff of 96.0 Ry, corresponding to a real-space grid spacing of 0.17 Å, were used for the calculations. A Troullier-Martins norm-conserving pseudopotential in Kleinman-Bylander form was employed<sup>54,55</sup>. Throughout this study, 256 stochastic orbitals were used, regardless of the number of atoms, and 10 uniformly distributed energy windows were utilized in the ew-sDFT and ew-efsDFT calculations. All statistical quantities were obtained using 5 independent runs, unless explicitly stated otherwise.

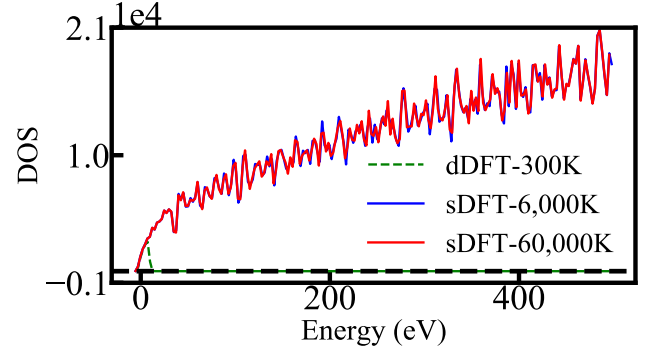


FIG. 2. The density of states of  $\text{Al}_{256}$  at different electron temperatures are shown in this figure. The green dashed line is the density of states calculated from dDFT. The solid blue line and the solid red line are calculated from sDFT at temperature 6,000K and 60,000K with Eq.(8).

Previous work by White and Collins has demonstrated the advantages of sDFT in studying warm dense matter.<sup>39</sup> The deterministic DFT (dDFT) calculations lack information on KS orbitals with high orbital energies. Therefore, evaluating properties which requires knowledge of high energy orbitals, like electron density of states, is not possible with dDFT. In Fig.2, we demonstrate that sDFT is capable of estimating the electronic density of states even at extremely high energies. This is necessary for studying warm dense matter with high electron temperatures. Similar results were observed by

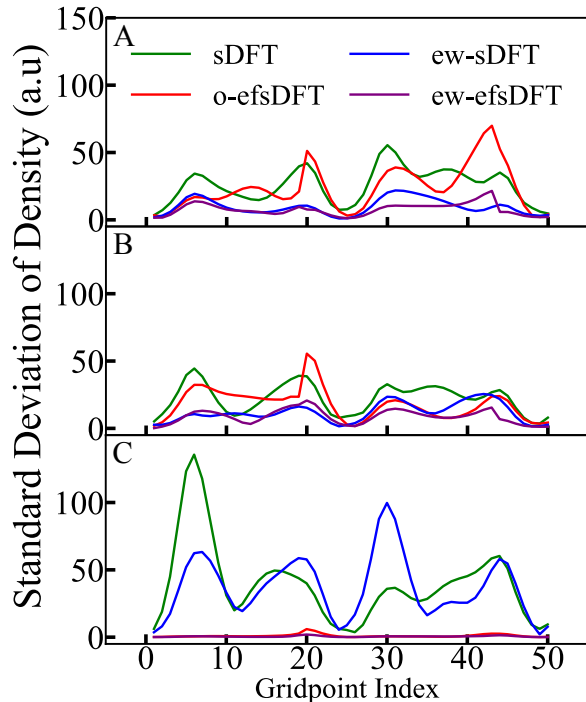


FIG. 3. This figure shows standard deviations (STD) of the density in sDFT and noise reduction techniques at different temperatures. We obtained the STDs over 5 independent trials for sDFT (green), ew-sDFT (blue), o-ef-sDFT (red), and ew-ef-sDFT (purple) at 300K (A), 6,000K (B), and 60,000K (C). We plotted the STDs for the first 50 grid points along the x-axis with  $y = z = 0.0$  of  $\text{Al}_{256}$ .

Fig.3 shows the standard deviations (STD) of the electron densities calculated with various sDFT implementations at different electron temperatures. Panel A demonstrates that real-space fragmentation is not capable of reducing noise in electron density at low electron temperatures; specifically, the noise from o-efsDFT is comparable to that from sDFT, and the noise from ew-efsDFT is comparable to that from ew-sDFT. On the other hand, the energy window method works reasonably well and can reduce the noise in electron density by almost 50%. This qualitative noise reduction performance is similar when the electron temperature is increased to 6000 K, as demonstrated in Fig.3, Panel B. Since the Fermi-Dirac function becomes smoother at higher electron temperatures, the overlap between two neighboring energy windows becomes larger. Therefore, both ew-sDFT and ew-efsDFT become less effective at reducing noise. Real-space fragmentation still cannot efficiently reduce noise in electron density at 6000 K. When the electron temperature is increased to 60,000 K, the efficiency of noise reduction becomes very different, as shown in Panel C of Fig.3. First, all real-space-fragmentation-based methods, including o-efsDFT and ew-efsDFT, can significantly reduce noise in electron density. The efficiency changes for real-space fragmentation methods will be explained in the following paragraph. Second, using only ew-sDFT is not capable of reducing noise in the electron density because there is a significant overlap between two neigh-

boring window functions.

It has been demonstrated that the noise reduction efficiency of real-space fragmentation methods depends on the difference between the fragment density matrix  $\sum_f \hat{\rho}_f$  and the system density matrix  $\hat{\rho}$ .<sup>45,46</sup> The difference between  $\sum_f \hat{\rho}_f$  and  $\hat{\rho}$  arises for two reasons. First, a  $\Gamma$ -point calculation is performed for each fragment. The finite size error from using a small supercell in a fragment DFT calculation is one reason for the discrepancy between  $\sum_f \hat{\rho}_f$  and  $\hat{\rho}$ . Second, the fragment density matrix  $\hat{\rho}_f$  is truncated at the boundary of  $D_f$ , according to Eq.(10). At 300 K,  $\hat{\rho}_f$  is very sensitive to fragment size, which can be confirmed by performing a unit cell calculation with k-point sampling. At this temperature, DFT calculations converge slowly with an increasing number of k-points (see Fig.S1 in the Supplemental Information). Also,  $\hat{\rho}_f$  is highly delocalized at 300 K, as shown in Fig.4, leading to a large truncation error at the boundary of  $D_f$ . However, at 60,000 K, fragment DFT calculations converge quickly with an increasing number of k-points, and  $\hat{\rho}_f$  decays to zero much faster (see Fig.4). Therefore, using a small supercell in a fragment DFT calculation results in  $\sum_f \hat{\rho}_f$  that is similar to  $\hat{\rho}$ . Errors associated with truncating  $\hat{\rho}_f$  are also negligible at 60,000 K.

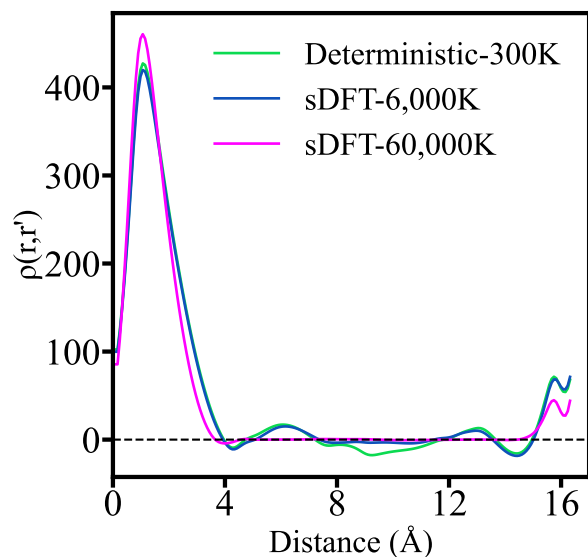


FIG. 4. One-dimensional slices of density matrix is shown in this figure. The green line is the results from a 300K deterministic DFT calculation while the blue/magenta line is from a sDFT calculation at 6000 K/60000 K. Details of calculating the density matrix are presented in the support information.

Noise reduction techniques can also be applied to other ground state properties like ground state energy and atomic forces. We list different energy terms calculated with various methods at different temperatures in Table I. We would like to emphasize that the reason we display results only up to 20,000 K is due in part to deterministic calculations of  $\text{Al}_{256}$  at a temperatures higher than 20,000 K is highly challenging. For all ground state energies, including those for sDFT above 20,000 K, please refer to Table S1 in the Supplemental In-

TABLE I. The average energies per electron and corresponding standard deviations (STD) for various sDFT methods at different temperatures. The statistics were obtained from 5 independent trials for each method of sDFT used in this study. In order, the kinetic energy ( $E_K$ ), non-local pseudopotential energy ( $E_{nl}$ ), local pseudopotential energy ( $E_{loc}$ ), hartree energy ( $E_H$ ), exchange-correlation energy ( $E_{XC}$ ), entropy ( $TS_{KS}$ ), and total energy ( $E_{tot}$ ) are shown in units of eV in the table. Each entry represents the average energy up to 4 decimal places and in parenthesis next to it, is the STD on the order of 0.1 meV.

Temperature(K)	Method	$E_K$	$E_{nl}$	$E_{loc}$	$E_H$	$E_{XC}$	$TS_{KS}$	$E_{tot}$
300	Deterministic	7.7052	-0.3639	5.4858	0.0381	-6.8521	-0.0011	-18.7095
	sDFT	7.7215(154)	-0.3666(12)	5.4858(16)	0.0494(3)	-6.8582(7)	-0.0009(0)	-18.6905(140)
	ew-sDFT	7.7059(124)	-0.3645(11)	5.4863(5)	0.0397(2)	-6.8531(2)	-0.0011(0)	-18.7084(110)
	o-efsDFT	7.7063(26)	-0.3643(3)	5.4871(13)	0.0434(2)	-6.8598(4)	-0.0010(0)	-18.7098(18)
	ew-efsDFT	7.7097(27)	-0.3643(5)	5.4861(3)	0.0385(2)	-6.8528(2)	-0.0011(0)	-18.7054(24)
6,000	Deterministic	7.7702	-0.3733	5.4846	0.0395	-6.8534	-0.1193	-18.7731
	sDFT	7.8035(250)	-0.3763(14)	5.4854(12)	0.0505(2)	-6.8595(3)	-0.1198(7)	-18.7377(227)
	ew-sDFT	7.7842(205)	-0.3747(16)	5.4853(8)	0.0431(2)	-6.8556(3)	-0.1196(8)	-18.7587(191)
	o-efsDFT	7.7696(45)	-0.3735(6)	5.4852(9)	0.0424(3)	-6.8576(4)	-0.1194(10)	-18.7748(40)
	ew-efsDFT	7.7739(24)	-0.3737(3)	5.4846(3)	0.0401(1)	-6.8543(1)	-0.1199(11)	-18.7706(15)
20,000	Deterministic	8.4300	-0.4342	5.4795	0.0368	-6.8528	-1.3115	-19.3737
	sDFT	8.4596(196)	-0.4372(16)	5.4803(10)	0.0482(4)	-6.8599(4)	-1.3159(30)	-19.3464(193)
	ew-sDFT	8.4677(230)	-0.4375(17)	5.4798(10)	0.0452(6)	-6.8582(5)	-1.3161(36)	-19.3407(200)
	o-efsDFT	8.4311(22)	-0.4344(4)	5.4797(2)	0.0373(1)	-6.8538(1)	-1.3144(28)	-19.3760(32)
	ew-efsDFT	8.4300(37)	-0.4342(3)	5.4797(1)	0.0370(0)	-6.8532(1)	-1.3145(38)	-19.3766(52)

formation. Some energy terms, such as local pseudopotential energy, Hartree energy, and exchange-correlation energy, can be directly evaluated with electron density. The noise in these energy terms is consistent with the noise in electron density. At 300 K, the noise reduction efficiency of o-efsDFT is limited, while o-efsDFT can significantly reduce noise at 20,000 K. ew-sDFT works well at 300 K, and its noise reduction efficiency is dramatically reduced at 20,000 K. For  $E_{loc}$ ,  $E_H$ , and  $E_{XC}$ , ew-efsDFT performs best at all three temperatures.

Kinetic energy and non-local pseudopotential energy can be calculated using Eq. (7). Noise reduction methods for these energy terms have been developed in previous studies<sup>44-46</sup>. Real-space-fragmentation-based methods, such as o-efsDFT and ew-efsDFT, have demonstrated significant noise reduction in these energy terms. However, ew-sDFT can only achieve marginal noise reduction, even at low electron temperatures. Previous studies have indicated that, at low electron temperatures, ew-sDFT can not reduce the noise in  $\text{Tr}(\hat{\rho}\hat{O})$  only if the matrix representation of  $\hat{O}$  is diagonal-dominant in the deterministic Kohn-Sham (KS) orbital basis<sup>44</sup>. Our results suggest that the kinetic operator  $\hat{t}$  and the non-local pseudopotential operator  $\hat{v}_{nl}$  tend to be diagonal-dominant in the deterministic KS orbital basis for the tested system.

Noise in the electron entropy term,  $S_{KS}$ , originates from two primary sources. The first source is the noise in electron density, which leads to noise in the Kohn-Sham Hamiltonian,  $\hat{h}_{KS}$ , and subsequently in the density matrix,  $\hat{\rho}$ . The second source is inherent in the stochastic trace formula used to calculate entropy. Despite significant reductions in electron density noise through methods such as o-efsDFT, ew-sDFT, and ew-efsDFT, we observe that noise in  $TS_{KS}$  persists. This observation indicates that the dominant noise contribution arises from the stochastic trace formula rather than electron density fluctuations. To delve deeper into this issue, we utilized

converged electron densities,  $\rho_{sDFT}$ , from sDFT or its noise-reduced variants, and performed a deterministic diagonalization of  $\hat{h}_{KS}[\rho_{sDFT}]$  to evaluate Eq. (9). This deterministic trace approach revealed a decrease in entropy noise when employing noise reduction techniques (see Table S2 in the Supplemental Information). This outcome underscores that the primary source of entropy noise is the stochastic trace formula, overshadowing the impact of noise reduction in electron density. Addressing the noise in the stochastic trace formula for entropy thus necessitates further research and development. Nevertheless, our findings indicate that the presence of significant noise in the entropy term does not adversely affect the accuracy of calculated electron densities and atomic forces.

In addition to noise-related challenges, we also identified the presence of bias or systematic errors in certain energy terms, particularly those that are non-linear functionals of electron density<sup>56</sup>. Notably, bias is evident in  $E_H$ ,  $E_{XC}$ , and  $TS_{KS}$ . Such biases are inherent to sDFT calculations, where, for instance,  $E_H$  obtained from sDFT is significantly higher compared to dDFT calculations, despite relatively small fluctuations in  $E_H$ . Noise-reduction methods play a crucial role in mitigating these biases, largely due to their effectiveness in minimizing fluctuations in electron density. Specifically, the systematic error in all energy terms is notably reduced when employing ew-efsDFT.

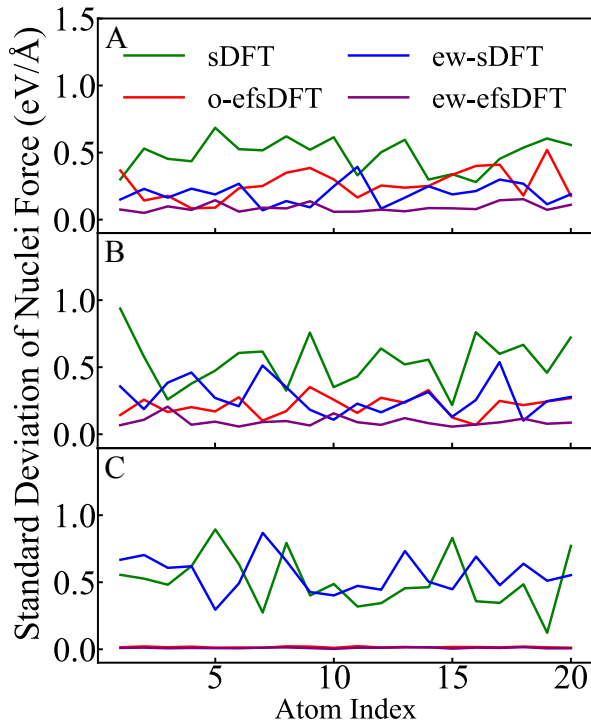


FIG. 5. Standard deviations (STD) of the total nuclei force ( $\text{eV}/\text{\AA}$ ) in sDFT and noise reduction techniques at different electron temperatures. We obtained the STD over 5 independent trials for sDFT (green), ew-sDFT (blue), o-ef-sDFT (red), and ew-ef-sDFT (purple) at 300 K (A), 6,000 K (B), and 60,000 K (C). We plotted the STDs for the first 20 atoms of  $\text{Al}_{256}$ .

Reducing noise in atomic forces is very important for determining equilibrium structures.<sup>57,58</sup> In Fig. 5, the STD of the force on the nuclei along the x-axis ( $F_x$ ) for the first 20 atoms is plotted for sDFT and noise reduction methods at electron temperatures of 300 K (Panel A), 6,000 K (Panel B), and 60,000 K (Panel C). At 300K, both o-efsDFT and ew-sDFT can marginally improve the fluctuation of nuclear forces, while ew-efsDFT performs best at 300 K. At 60,000 K, ew-sDFT is not capable of reducing noise in nuclear forces. However, both methods, o-efsDFT and ew-efsDFT, can significantly reduce the noise in nuclear forces at 60,000 K. This is consistent with the noise reduction efficiency observed in electron density at different temperatures. In Fig. 6, we highlight the efficiency of sDFT and noise reduction techniques by plotting the average STD of nuclear forces along the x-axis as a function of temperature. The efficiency of ew-sDFT is consistent with the work done by Hadad et al.<sup>42</sup>

To investigate the impact of system size on the noise reduction efficiency of sDFT and ew-efsDFT, we conducted a series of tests focusing on the atomic forces within different-sized systems. Our tests involved analyzing data from five independent trials for both sDFT and ew-efsDFT across a range of system sizes. However, due to resource constraints, we were limited to single runs for  $\text{Al}_{500}$  and  $\text{Al}_{864}$  when using

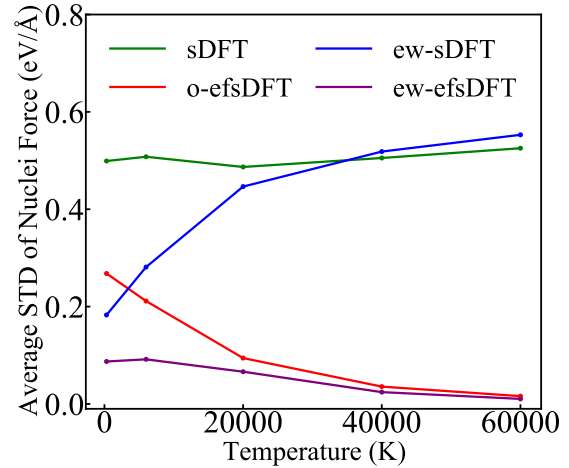


FIG. 6. Noise reduction efficiency in nuclei forces ( $\text{eV}/\text{\AA}$ ) of various sDFT methods with respect to temperature. We obtained the standard deviation (STD) of atomic force on each atom over 5 independent trials for each method at 300 K, 6000 K, 20,000 K, 40,000 K, and 60,000 K. We then average all STDs of different atoms and plotted the corresponding values for sDFT (green), ew-sDFT (blue), o-ef-sDFT (red), and ew-ef-sDFT (purple).

ew-efsDFT. Given these limitations, it was crucial to validate the reliability of our statistical analysis on the atomic forces for these larger systems. To achieve this, we employed two distinct statistical methods for smaller system sizes, which served as a basis for comparison. The first method calculated the STD of the force on each atom across the independent trials, providing a measure of variability for individual atomic forces. The second method aggregated the forces from all atoms within a single trial and then calculated the STD, offering a holistic view of force variability within a single system snapshot. Our findings, presented in Table II, reveal no significant difference between the results obtained from these two statistical approaches. This consistency suggests that, for larger systems where conducting multiple calculations is not feasible due to resource constraints, a single calculation can reliably represent the statistical behavior of atomic forces. This insight is particularly valuable for efficiently assessing the noise reduction efficiency of sDFT and ew-efsDFT in large-scale systems, indicating that even with limited data, meaningful statistical conclusions can be drawn. We want to emphasize that the equivalence of the two statistical methods may only be applicable to a crystal structure, where atoms are equivalent in such a system. We do not recommend calculating STD across different atoms in a slab model or a nanocrystal. Aside from the sDFT  $\text{Al}_4$  results in Table II, which could be the result of artifacts from using a single unit cell, there appear to be no significant changes in the efficiency of noise reduction in response to system size. Since the number of stochastic orbitals is kept constant across all calculations, this suggests that the number of stochastic orbitals needed for a system is nearly independent of the system size.

TABLE II. Comparison of different methods of obtaining statistics for nuclei forces (eV/Å). Here we compare using sDFT and ewf-sDFT on various system sizes of Al all of which were ran at an electron temperature of 6,000K. The Numbers reported in column A was a result of taking the STD across all atoms for each trial, then taking the average of those STDs. Numbers reported in column B was a result of taking the STD for each atom across all trials, then taking the average of those STDs. For Al<sub>500</sub> and Al<sub>864</sub>, statistics were obtained from only B.

Temperature(K)	Method	System	A	B	
6,000	sDFT	Al <sub>4</sub>	0.3258	0.3332	
		Al <sub>32</sub>	0.6225	0.5257	
		Al <sub>108</sub>	0.5605	0.4764	
		Al <sub>256</sub>	0.6051	0.5078	
	ew-efsDFT	Al <sub>108</sub>	0.1193	0.1024	
		Al <sub>256</sub>	0.1078	0.0917	
		Al <sub>500</sub>	—	0.1097	
		Al <sub>864</sub>	—	0.1146	
	60,000	sDFT	Al <sub>4</sub>	0.3434	0.3476
			Al <sub>32</sub>	0.6756	0.5861
Al <sub>108</sub>			0.5939	0.5079	
Al <sub>256</sub>			0.6222	0.5253	
ew-efsDFT		Al <sub>108</sub>	0.0165	0.0140	
		Al <sub>256</sub>	0.0122	0.0104	
		Al <sub>500</sub>	—	0.0154	
		Al <sub>864</sub>	—	0.0170	

Given the performance of ew-efsDFT in noise reduction for properties such as density, ground-state energy, and force on nuclei, we tested its computational efficiency for larger systems. Our tests were conducted on the Cori-KNL and Perlmutter supercomputers at the National Energy Research Scientific Computing Center (NERSC). Calculations on Cori-KNL included Al<sub>256</sub>, Al<sub>500</sub>, and Al<sub>864</sub> at 900 K and 6,000 K. The same set of system sizes was tested on Perlmutter, but at a system temperature of 60,000 K. The system parameters defined earlier in the discussion were applied to all six runs. In Fig.7 and Fig.8, we plotted the total and per iteration CPU time per core versus the number of electrons in the system on a log-log scale. The top panel of Fig.7 presents the results for the runs at 6,000 K, which shows that the time needed for each iteration scales as  $O(N_e^{0.83})$ , while the time needed for a single calculation scales as  $O(N_e^{0.91})$ . The bottom panel of Fig.7 displays the results for the runs at 900 K, indicating that the time needed for each iteration scales as  $O(N_e^{0.86})$ , while the time needed for a single calculation scales as  $O(N_e^{0.62})$ . In Fig.8, the run conducted on Perlmutter at 60,000 K showed that the time needed for each iteration scales as  $O(N_e^{0.63})$ , and the time needed for a single calculation scales as  $O(N_e^{0.96})$ . We continue to observe similar scaling on different computational architectures, and the scaling does not seem to be impacted by system size or electron temperature.

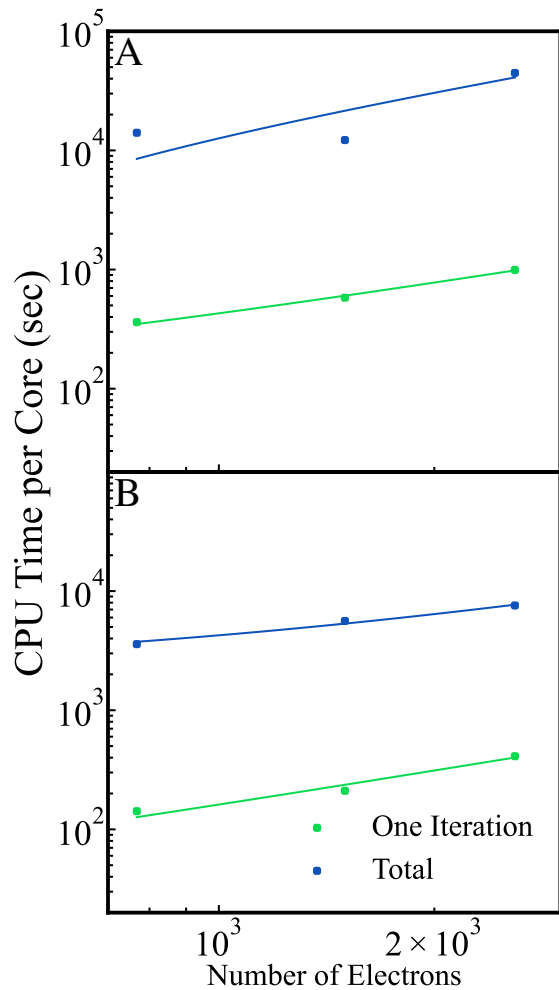


FIG. 7. Scaling of ew-efsDFT at 900 K and 6,000 K on NERSC Corri-KNL. In panels A (6,000 K) and B (900 K), the average time it took to complete one SCF iteration (blue) and the total time (green) to converge the SCF calculations were plotted against their corresponding system size.

Fig.(8) suggests that our noise reduction method, ew-efsDFT, is significantly different from the mixed stochastic density functional theory (MDFT) developed by White and Collins.<sup>39</sup> In MDFT, stochastic orbitals are used to correct a dDFT calculation at a lower electron temperature. Therefore, the scaling of MDFT is still limited by the need to perform a dDFT calculation for the whole system. In contrast, ew-efsDFT uses stochastic orbitals to correct a reference system composed of fragments. By taking advantage of the localized density matrix at high electron temperatures, the noise reduction efficiency of ew-efsDFT is significant, and linear scaling is still achieved at high electron temperatures. This enables the modeling of disordered warm dense matter with a large supercell.



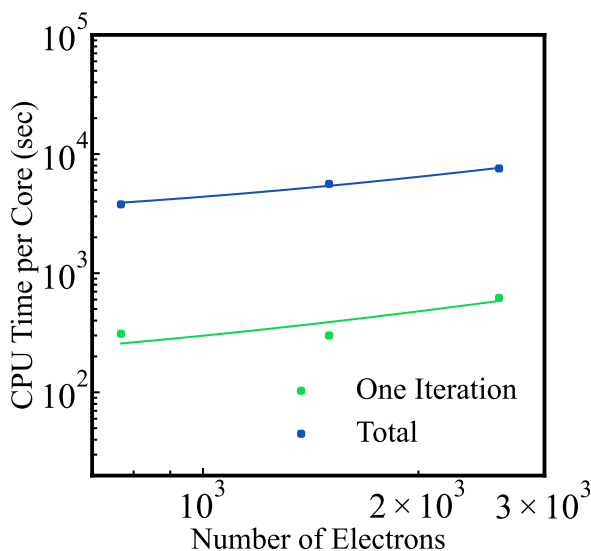


FIG. 8. Scaling of ew-efsDFT at 60,000 K on NERSC Perlmutter. The average time it took to complete one SCF iteration (blue) and the total time (green) to converge the SCF calculations were plotted against their corresponding system size.

#### IV. CONCLUSIONS

In this work, we present benchmark studies on noise-reduction techniques in stochastic density functional theory (sDFT) for metallic systems. Our findings indicate that the efficiency of noise reduction depends on the electron temperature. Specifically, at low electron temperatures, the energy-window-based method, ew-sDFT, outperforms the fragmentation-based approach, o-efsDFT. Conversely, at extremely high electron temperatures, o-efsDFT demonstrates superior performance over ew-efsDFT, attributed to the localized nature of the one-body density matrix. At both low and high electron temperatures, ew-efsDFT, which integrates both the energy-window and fragmentation approaches, emerges as the most efficient method. Our results further reveal that ew-efsDFT scales linearly, enabling the efficient simulation of large metallic systems across a large range of electron temperatures. Despite ew-efsDFT's current status as the most effective noise-reduction method, we observe significant residual noises in electron density, energy, and nuclear forces at low electron temperatures. This underscores the necessity for further advancements. Additionally, the development of a formula to mitigate noise in electron entropy is imperative to enhance the accuracy of total energy calculations at high electron temperatures.

#### DATA AVAILABILITY

The data that support the findings of this study are available from the corresponding author upon reasonable request.

#### SUPPLEMENTARY MATERIAL

Discussions on convergence of electronic structure with system size and electron temperatures are included in the Supplementary Material<sup>59,60</sup>. The Supplementary Material also includes a complete data on energies per electron with different electron temperatures, analysis of noise in entropy, and details in calculating the density matrix.

#### V. ACKNOWLEDGMENTS

J. V. and M. C. gratefully acknowledges support from the National Science Foundation EAR-2246687. Resources of the National Energy Research Scientific Computing Center (NERSC), a U.S. Department of Energy Office of Science User Facility operated under Contract No. DE-AC02-05CH11231, are greatly acknowledged.

- <sup>1</sup>A. Bhaduri, *Mechanical Properties and Working of Metals and Alloys*, Springer Series in Materials Science (Springer Nature Singapore, 2018).
- <sup>2</sup>M. E. McHenry and D. E. Laughlin, "19 - magnetic properties of metals and alloys," in *Physical Metallurgy (Fifth Edition)*, edited by D. E. Laughlin and K. Hono (Elsevier, Oxford, 2014) fifth edition ed., pp. 1881–2008.
- <sup>3</sup>H. Ehrenreich and L. Schwartz, "The electronic structure of alloy," *Solid State Phys.*, **31**, 149–286 (1976).
- <sup>4</sup>J. Aarons, M. Sarwar, D. Thompsett, and C.-K. Skylaris, "Perspective: Methods for large-scale density functional calculations on metallic systems," *J. Chem. Phys.* **145**, 220901 (2016).
- <sup>5</sup>C. J. Herring and M. M. Montemore, "Recent advances in real-time time-dependent density functional theory simulations of plasmonic nanostructures and plasmonic photocatalysis," *ACS Nanosci. Au* **3**, 269–279 (2023).
- <sup>6</sup>J. W. D. Connolly and A. R. Williams, "Density-functional theory applied to phase transformations in transition-metal alloys," *Phys. Rev. B* **27**, 5169–5172 (1983).
- <sup>7</sup>J. Greeley, J. K. Nørskov, and M. Mavrikakis, "Electronic structure and catalysis on metal surfaces," *Annu. Rev. Phys. Chem.* **53**, 319–348 (2002).
- <sup>8</sup>Z. Zhang, C. Zhang, H. Zheng, and H. Xu, "Plasmon-driven catalysis on molecules and nanomaterials," *Acc. Chem. Res.* **52**, 2506–2515 (2019).
- <sup>9</sup>X. Gao, R. Chen, T. Liu, H. Fang, G. Qin, Y. Su, and J. Guo, "High-entropy alloys: a review of mechanical properties and deformation mechanisms at cryogenic temperatures," *J. Mater. Sci.* **57**, 6573–6606 (2022).
- <sup>10</sup>U. Banin, Y. Ben-Shahar, and K. Vinokurov, "Hybrid semiconductor–metal nanoparticles: From architecture to function," *Chem. Mater.* **26**, 97–110 (2014).
- <sup>11</sup>A. H. Hakimioun, B. D. Vandegehuchte, D. Curulla-Ferre, K. Kaźmierczak, P. N. Plessow, and F. Studt, "Metal–support interactions in heterogeneous catalysis: Dft calculations on the interaction of copper nanoparticles with magnesium oxide," *ACS Omega* **8**, 10591–10599 (2023).
- <sup>12</sup>D. Stradi, U. Martinez, A. Blom, M. Brandbyge, and K. Stokbro, "General atomistic approach for modeling metal–semiconductor interfaces using density functional theory and nonequilibrium green's function," *Phys. Rev. B* **93**, 155302 (2016).
- <sup>13</sup>J. Aarons, L. Jones, A. Varambhia, K. E. MacArthur, D. Ozkaya, M. Sarwar, C.-K. Skylaris, and P. D. Nellist, "Predicting the oxygen-binding properties of platinum nanoparticle ensembles by combining high-precision electron microscopy and density functional theory," *Nano Lett.* **17**, 4003–4012 (2017), pMID: 28644034.
- <sup>14</sup>M. Koenig, A. Benuzzi-Mounaix, A. Ravasio, T. Vinci, N. Ozaki, S. Lepape, D. Batani, G. Huser, T. Hall, D. Hicks, *et al.*, "Progress in the study of warm dense matter," *Plasma Phys. Control. Fusion* **47**, B441 (2005).
- <sup>15</sup>J. C. Smith, F. Sagredo, and K. Burke, "Warming up density functional theory," in *Frontiers of Quantum Chemistry*, edited by M. J. Wójcik, H. Nakatsuji, B. Kirtman, and Y. Ozaki (Springer Singapore, Singapore, 2018) pp. 249–271.

- <sup>16</sup>A. Blanchet, M. Torrent, and J. Clerouin, “Requirements for very high temperature kohn–sham dft simulations and how to bypass them,” *Phys. Plasmas* **27**, 122706 (2020).
- <sup>17</sup>T. Zhu, W. Pan, and W. Yang, “Structure of solid-state systems from embedded-cluster calculations: A divide-and-conquer approach,” *Phys. Rev. B* **53**, 12713–12724 (1996).
- <sup>18</sup>J. C. Prentice, J. Aarons, J. C. Womack, A. E. Allen, L. Andrinopoulos, L. Anton, R. A. Bell, A. Bhandari, G. A. Bramley, R. J. Charlton, *et al.*, “The onetep linear-scaling density functional theory program,” *J. Chem. Phys.* **152**, 174111 (2020).
- <sup>19</sup>W. Kohn, “Density functional and density matrix method scaling linearly with the number of atoms,” *Phys. Rev. Lett.* **76**, 3168 (1996).
- <sup>20</sup>T. A. Wesolowski and Y. A. Wang, *Recent Progress in Orbital-free Density Functional Theory* (WORLD SCIENTIFIC, 2013).
- <sup>21</sup>E. Artacho, D. Sánchez-Portal, P. Ordejón, A. Garcia, and J. M. Soler, “Linear-scaling ab-initio calculations for large and complex systems,” *Phys. Status Solidi (b)* **215**, 809–817 (1999).
- <sup>22</sup>E. Hernández, M. Gillan, and C. Goringe, “Linear-scaling density-functional-theory technique: the density-matrix approach,” *Phys. Rev. B* **53**, 7147 (1996).
- <sup>23</sup>T. M. Henderson, “Embedding wave function theory in density functional theory,” *J. Chem. Phys.* **125** (2006).
- <sup>24</sup>P. Huang and E. A. Carter, “Advances in correlated electronic structure methods for solids, surfaces, and nanostructures,” *Annu. Rev. Phys. Chem.* **59**, 261–290 (2008).
- <sup>25</sup>J. M. Soler, E. Artacho, J. D. Gale, A. García, J. Junquera, P. Ordejón, and D. Sánchez-Portal, “The siesta method for ab initio order-n materials simulation,” *J. Phys. Condens. Matter* **14**, 2745 (2002).
- <sup>26</sup>A. Krishtal, D. Sinha, A. Genova, and M. Pavanello, “Subsystem density-functional theory as an effective tool for modeling ground and excited states, their dynamics and many-body interactions,” *J. Phys. Condens. Matter* **27**, 183202 (2015).
- <sup>27</sup>W. Yang, “Direct calculation of electron density in density-functional theory,” *Phys. Rev. Lett.* **66**, 1438–1441 (1991).
- <sup>28</sup>C. R. Jacob and J. Neugebauer, “Subsystem density-functional theory,” *Wiley Interdiscip. Rev. Comput. Mol. Sci.* **4**, 325–362 (2014).
- <sup>29</sup>T. A. Wesolowski, S. Shedge, and X. Zhou, “Frozen-density embedding strategy for multilevel simulations of electronic structure,” *Chem. Rev.* **115**, 5891–5928 (2015).
- <sup>30</sup>W. Kohn, “Density functional and density matrix method scaling linearly with the number of atoms,” *Phys. Rev. Lett.* **76**, 3168–3171 (1996).
- <sup>31</sup>A. Schindlmayr, “Decay properties of the one-particle green function in real space and imaginary time,” *Phys. Rev. B* **62**, 12573–12576 (2000).
- <sup>32</sup>R. Baer and M. Head-Gordon, “Sparsity of the density matrix in kohn-sham density functional theory and an assessment of linear system-size scaling methods,” *Phys. Rev. Lett.* **79**, 3962 (1997).
- <sup>33</sup>M. Challacombe, “A simplified density matrix minimization for linear scaling self-consistent field theory,” *J. Chem. Phys.* **110**, 2332–2342 (1999).
- <sup>34</sup>M. Benzi, P. Boito, and N. Razouk, “Decay properties of spectral projectors with applications to electronic structure,” *SIAM J. Matrix Anal. Appl.* **33**, 1299–1322 (2012).
- <sup>35</sup>S. Ismail-Beigi and T. Arias, “Locality of the density matrix in metals, semiconductors, and insulators,” *Phys. Rev. Lett.* **82**, 2127 (1999).
- <sup>36</sup>S. Ismail-Beigi and T. A. Arias, “Locality of the density matrix in metals, semiconductors, and insulators,” *Phys. Rev. Lett.* **82**, 2127 (1999).
- <sup>37</sup>J. Sun, R. C. Remsing, Y. Zhang, Z. Sun, A. Ruzsinszky, H. Peng, Z.-H. Yang, A. Paul, U. Waghmare, X. Wu, M. Klein, and J. Perdew, “Accurate first-principles structures and energies of diversely bonded systems from an efficient density functional,” *Nat. Chem.* **8**, 831–836 (2016).
- <sup>38</sup>C.-K. Skylaris, P. D. Haynes, A. A. Mostofi, and M. C. Payne, “Introducing onetep: Linear-scaling density functional simulations on parallel computers,” *J. Chem. Phys.* **122**, 084119 (2005).
- <sup>39</sup>A. J. White and L. A. Collins, “Fast and universal kohn-sham density functional theory algorithm for warm dense matter to hot dense plasma,” *Phys. Rev. Lett.* **125**, 055002 (2020).
- <sup>40</sup>R. Baer, D. Neuhauser, and E. Rabani, “Self-averaging stochastic kohn-sham density-functional theory,” *Phys. Rev. Lett.* **111**, 106402 (2013).
- <sup>41</sup>Y. Cytter, E. Rabani, D. Neuhauser, and R. Baer, “Stochastic density functional theory at finite temperatures,” *Phys. Rev. B* **97**, 115207 (2018).
- <sup>42</sup>R. E. Hadad, A. Roy, E. Rabani, R. Redmer, and R. Baer, “Stochastic density functional theory combined with langevin dynamics for warm dense matter,” (2024), arXiv:2401.11336.
- <sup>43</sup>Q. Liu and M. Chen, “Plane-wave-based stochastic-deterministic density functional theory for extended systems,” *Phys. Rev. B* **106**, 125132 (2022).
- <sup>44</sup>M. Chen, R. Baer, D. Neuhauser, and E. Rabani, “Energy window stochastic density functional theory,” *J. Chem. Phys.* **151**, 114116 (2019).
- <sup>45</sup>M. Chen, R. Baer, D. Neuhauser, and E. Rabani, “Overlapped embedded fragment stochastic density functional theory for covalently-bonded materials,” *J. Chem. Phys.* **150**, 034106 (2019).
- <sup>46</sup>M. Chen, R. Baer, D. Neuhauser, and E. Rabani, “Stochastic density functional theory: Real- and energy-space fragmentation for noise reduction,” *J. Chem. Phys.* **154**, 204108 (2021).
- <sup>47</sup>R. Kosloff, “Time-dependent quantum-mechanical methods for molecular dynamics,” *J. Phys. Chem.* **92**, 2087–2100 (1988).
- <sup>48</sup>R. Kosloff, “Propagation methods for quantum molecular dynamics,” *Annu. Rev. Phys. Chem.* **45**, 145–178 (1994).
- <sup>49</sup>A. D. Becke, “Density-functional exchange-energy approximation with correct asymptotic behavior,” *Phys. Rev. A* **38**, 3098–3100 (1988).
- <sup>50</sup>C. Lee, W. Yang, and R. G. Parr, “Development of the colle-salvetti correlation-energy formula into a functional of the electron density,” *Phys. Rev. B* **37**, 785–789 (1988).
- <sup>51</sup>Z. A. Moldabekov, M. Lokamani, J. Vorberger, A. Cangi, and T. Dornheim, “Non-empirical mixing coefficient for hybrid xc functionals from analysis of the xc kernel,” *J. Phys. Chem. Lett.* **14**, 1326–1333 (2023).
- <sup>52</sup>T. Dornheim, S. Groth, and M. Bonitz, “The uniform electron gas at warm dense matter conditions,” *Phys. Rep.* **744**, 1–86 (2018).
- <sup>53</sup>M. Bonitz, T. Dornheim, Z. A. Moldabekov, S. Zhang, P. Hamann, H. Kählert, A. Filinov, K. Ramakrishna, and J. Vorberger, “Ab initio simulation of warm dense matter,” *Phys. Plasmas* **27**, 042710 (2020).
- <sup>54</sup>N. Troullier and J. L. Martins, “Efficient pseudopotentials for plane-wave calculations,” *Phys. Rev. B* **43**, 1993 (1991).
- <sup>55</sup>L. Kleinman and D. Bylander, “Efficacious form for model pseudopotentials,” *Phys. Rev. Lett.* **48**, 1425 (1982).
- <sup>56</sup>M. D. Fabian, B. Shpiro, E. Rabani, D. Neuhauser, and R. Baer, “Stochastic density functional theory,” *Wiley Interdiscip. Rev. Comput. Mol. Sci.* **9**, e1412 (2019).
- <sup>57</sup>E. Armon, E. Rabani, D. Neuhauser, and R. Baer, “Efficient langevin dynamics for “noisy” forces,” *J. Chem. Phys.* **152** (2020).
- <sup>58</sup>M. Chen, R. Baer, and E. Rabani, “Structure optimization with stochastic density functional theory,” *J. Chem. Phys.* **158** (2023).
- <sup>59</sup>P. Giannozzi, S. Baroni, N. Bonini, M. Calandra, R. Car, C. Cavazzoni, D. Ceresoli, G. L. Chiarotti, M. Cococcioni, I. Dabo, A. Dal Corso, S. Fabris, G. Fratesi, S. de Gironcoli, R. Gebauer, U. Gerstmann, C. Gougoussis, A. Kokalj, M. Lazzeri, L. Martin-Samos, N. Marzari, F. Mauri, R. Mazzarello, S. Paolini, A. Pasquarello, L. Paulatto, C. Sbraccia, S. Scandolo, G. Sclauzero, A. P. Seitsonen, A. Smogunov, P. Umari, and R. M. Wentzcovitch, “Quantum espresso: a modular and open-source software project for quantum simulations of materials,” *J. Phys. Condens. Matter* **21**, 395502 (2009).
- <sup>60</sup>P. Giannozzi, O. Andreussi, T. Brumme, O. Bunau, M. Buongiorno Nardelli, M. Calandra, R. Car, C. Cavazzoni, D. Ceresoli, M. Cococcioni, N. Colonna, I. Carnimeo, A. Dal Corso, S. de Gironcoli, P. Delugas, R. A. J. DiStasio, A. Ferretti, A. Floris, G. Fratesi, G. Fugallo, R. Gebauer, U. Gerstmann, F. Giustino, T. Gorni, J. Jia, M. Kawamura, H.-Y. Ko, A. Kokalj, E. Küçükbenli, M. Lazzeri, M. Marsili, N. Marzari, F. Mauri, N. L. Nguyen, H.-V. Nguyen, A. Otero-de-la Roza, L. Paulatto, S. Poncé, D. Rocca, R. Sabatini, B. Santra, M. Schlipf, A. P. Seitsonen, A. Smogunov, I. Timrov, T. Thonhauser, P. Umari, N. Vast, X. Wu, and S. Baroni, “Advanced capabilities for materials modelling with quantum espresso,” *J. Phys. Condens. Matter* **29**, 465901 (2017).